

Changes in pore geometry and relative permeability caused by carbonate precipitation in porous media

Fei Jiang* and Takeshi Tsuji

International Institute for Carbon-Neutral Energy Research (WPI-I2CNER), Kyushu University, 744 Motoooka, Nishi-ku, Fukuoka 819-0395, Japan

(Received 26 January 2014; published 12 November 2014)

The CO₂ behavior within the reservoirs of carbon capture and storage projects is usually predicted from large-scale simulations of the reservoir. A key parameter in reservoir simulation is relative permeability. However, mineral precipitation alters the pore structure over time, and leads correspondingly to permeability changing with time. In this study, we numerically investigate the influence of carbonate precipitation on relative permeability during CO₂ storage. The pore spaces in rock samples were extracted by high-resolution microcomputed tomography (CT) scanned images. The fluid velocity field within the three-dimensional pore spaces was calculated by the lattice Boltzmann method, while reactive transport with calcite deposition was modeled by an advection-reaction formulation solved by the finite volume method. To increase the computational efficiency and reduce the processing time, we adopted a graphics processing unit parallel computing technique. The relative permeability of the sample rock was then calculated by a highly optimized two-phase lattice Boltzmann model. We also proposed two pore clogging models. In the first model, the clogging processes are modeled by transforming fluid nodes to solid nodes based on their precipitated mass level. In the second model, the porosity is artificially reduced by adjusting the gray scale threshold of the CT images. The developed method accurately simulates the mineralization process observed in laboratory experiment. Precipitation-induced evolution of pore structure significantly influenced the absolute permeability. The relative permeability, however, was much more influenced by pore reduction in the nonwetting phase than in the wetting phase. The output of the structural changes in pore geometry by this model could be input to CO₂ reservoir simulators to investigate the outcome of sequestered CO₂.

DOI: [10.1103/PhysRevE.90.053306](https://doi.org/10.1103/PhysRevE.90.053306)

PACS number(s): 02.60.-x, 91.60.Np, 91.60.Tn

I. INTRODUCTION

Geological CO₂ storage is considered a promising solution for reducing carbon emissions into the atmosphere. The mechanisms of geological CO₂ storage include structural and stratigraphic trapping, capillary trapping, dissolution trapping, and mineral trapping (mineral precipitation) [1]. CO₂ mineralization offers an attractive option for the permanent and safe storage of solid carbonates. CO₂ mineralization is expected to reduce the permeability of the reservoir and alter the behavior of the captured CO₂. However, since the mechanics of mineral formation remain poorly understood, the accuracy of quantitative assessments for mineralization and its influence to permeability is insufficient. Mineralization phenomena have been investigated by indirect measurements over a wide range of chemical compositions and under various reservoir conditions [2,3]. From the results of these experiments, researchers have elucidated geochemical reactions among CO₂, water, and rock minerals, and derived theoretical laws of calcite growth rate. Recently, *in situ* measurement techniques have been sufficiently improved to elucidate nanoscale crystal growth mechanisms [4–6]. These techniques have been intensively applied to understand how crystals grow from supersaturated solutions under representative hydrodynamic conditions. All of the above studies have focused on the fundamental physicochemical processes of CaCO₃ precipitation. Conversely, the effect of mineralization on the transport and flow properties of porous media has been largely

neglected [7,8]. The changes in solid phase volume induced by precipitation modify the rock structure of the medium. Consequently, the parameters that govern fluid behavior within the rock, such as permeability and relative permeability, should be altered by mineralization. Decreased permeability would mitigate injected CO₂ leakage and facilitate CO₂ storage in areas lacking continuous cap rock. Conversely, clogging of the reservoir would probably reduce injectivity. To identify the main factors responsible for injectivity reduction, Yoo *et al.* [9] performed flow experiments at various temperatures, pH, and reactant concentrations. Since the relative permeability plays an important role in predicting the outcome of injected CO₂ in large-scale reservoir simulations, the effect of mineralization on the relative permeability must be determined. However, the change in relative permeability induced by mineralization is difficult to measure, since CO₂ precipitation continuously evolves the rock microstructure. An alternative approach is to numerically simulate fluid transport through digitized rock samples that mimic the evolved microstructures. The purpose of this study is to numerically investigate the influence of carbonate precipitation on the relative permeability of CO₂ storing reservoirs.

The flow properties of the reservoir rock can be evaluated by the lattice Boltzmann method (LBM). LBM simulates single-phase and multiphase fluid flows through porous media [10,11], and it is eminently suitable for calculating the permeability of various rock types under different *in situ* conditions, because of its flexibility. LBM possesses several excellent features. It simplifies the handling of complex boundaries (can incorporate microscopic interactions) and flexibly reproduces the interface between multiple phases. These features are ideal

*Corresponding author: jiang@i2cner.kyushu-u.ac.jp

for simulating multiphase fluid flow through porous media. In the present study, we calculate the relative permeability using an optimized version of the color gradient multiphase lattice Boltzmann (LB) model with multiple-relaxation-time collision operator [12], which permits higher viscosity ratios and lower capillary numbers than the standard LB model.

Meanwhile, the carbonate precipitation process during CO₂ injection is typically modeled by reactive transport through porous media [13,14]. The LBM has also been extended and applied to multicomponent reactive transport problems [8,15,16]. In these LB modeling studies, the qualitative features of reactive transport were characterized in a simple numerical domain while varying the dimensionless Peclet (Pe) and Damköhler (Da) numbers. However, simulating carbonate precipitation processes in digitized rock microstructures remains a challenge. Imaging technology [e.g., microcomputed tomography (CT) scan and magnetic resonance imaging] has become sufficiently advanced to describe complex pore structures in rocks with high resolution. From such microstructural images, we can reconstruct digital rock models. Pore-scale simulation through high-resolution digital rock requires a large computational domain, which incurs high runtime and memory costs. This difficulty, however, can be overcome by a highly efficient parallel implementation using graphics processing unit architecture. To reduce the memory consumption and improve performance, the LB-based pore-scale transport model of carbonate precipitation was replaced by a simple finite volume method (FVM).

In this study, we develop a pore-scale numerical scheme for exploring the dynamics of porosity and relative permeability changes caused by carbonate precipitation in real rock microstructures. The rock geometric model is constructed using micro-CT scanned images of a Berea sandstone sample. Direct flow simulation on this reconstructed rock sample is carried out. By evaluating pore structure evolution due to precipitation, the changes in permeability can be calculated. In order to mimic the experiment by Yoo *et al.* [9] for comparison, we extended and improved their reactive transport model and adopted the same conditions. The aim of this paper is to investigate the effect of different precipitation patterns on both the absolute and relative permeability based on this developed mineralization model.

II. METHODS

The proposed mineralization simulation method contains four modules: (1) a reconstruction module for the geometric rock model, (2) an LB module that calculates the fluid velocity field inside the reservoir rock, (3) a finite volume reactive transport module for the advection and diffusion of the dissolved species, and (4) two types of clogging module that determine crystal growth. The geometric rock model is generated from micro-CT scanned images and input to the main solver. The fluid and reactive transport solvers are coupled through the velocity field. However, because the flow field and precipitation process operate on different time scales, we introduce two assumptions into our model. First, the flow field is evolved by LBM until it reaches steady state, and it is maintained constant during each time step for the reactive transport solver. Second, the geometry of the

solid is assumed unchanged during a single time step of the reactive transport. The clogging model updates the solid phase according to precipitation processes and consequently alters the geometry and porosity of the sample sandstone. In this module, a solid precipitate volume fraction is imposed. Finally, the relative permeability, which depends on the digital rock microstructures updated by the clogging modules, is separately calculated by a multiphase LBM solver at selected time steps.

A. Rock model

The geometrical datasets used in this study were extracted from a cylindrical core of Berea sandstone imaged by a multislice micro-CT scanner. The scanned images are resolved to 3.2 μm. The complete dataset contains 396 slices imaged at depth increments of 5 μm. In the image data, each pixel corresponds to one byte, storing a gray scale value (0–255) that represents the attenuation of the rock at that point. This value is proportional to the density of the material; the higher the value, the denser the pixel. The pore and mineral phases within the images are identified and labeled by a segmentation process. Here, we use a single gray scale threshold method which matches the typical porosity of the Berea sandstone (21%). The gray scale datasets are then binarized (with 0 and 1 denoting pore and solid grids, respectively). Subsequently, these segmented two-dimensional pixel images are linearly interpolated to generate a voxel-based three-dimensional volume with 3.2 μm resolution. The reconstructed three-dimensional geometry is shown in Fig. 1. The binary values stored in the rock matrix are directly loaded into the fluid and reactive transport solvers, forming a solid boundary for the simulations.

B. Flow solver

The single-phase and multiphase flows through the pore space are solved by LBM. The single-phase solver uses a standard single-relaxation-time (SRT) model [17], while the multiphase solver adopts an improved color gradient model with multiple-relaxation-time (MRT) collision operator [12]. The governing equation for LBM is given by

$$f_i(x + e_i \delta t, t + \delta t) = f_i(x, t) + \Omega_i, \quad i = 0, \dots, 18, \quad (1)$$

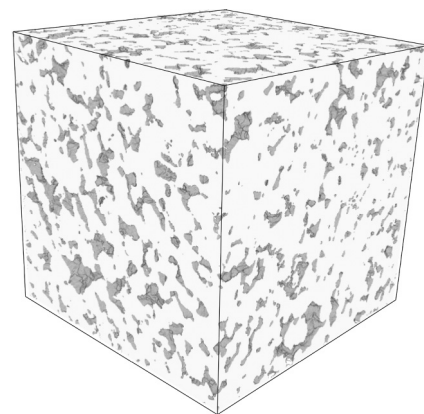


FIG. 1. Three-dimensional pore geometry of Berea sandstone reconstructed from scanned microcomputed tomography images. The physical size of this digital rock sample is 1.28 × 1.28 × 1.28 mm.

where δt is the time step and $f_i(x, t)$ is the particle distribution function that represents the probability of finding a particle at node \mathbf{x} and time t with velocity e_i . Here the D3Q19 model is adopted. Collision operators for MRT (Ω^{MRT}) and SRT (Ω^{SRT}) are given as the following equations:

$$\begin{aligned}\Omega^{\text{MRT}} &= \mathbf{M}^{-1} \mathbf{S} [(\mathbf{M}f) - \mathbf{m}^{\text{eq}}], \\ \Omega^{\text{SRT}} &= -\frac{1}{\tau} (f - f^{\text{eq}}),\end{aligned}\quad (2)$$

where \mathbf{M} is the transformation matrix which transforms the distributions into moment space. f^{eq} is the equilibrium particle distribution function [18]. The equilibrium vector \mathbf{m}^{eq} is composed of equilibrium moments and is calculated as [12]. The matrix \mathbf{S} is a diagonal collision matrix indicating the relaxation rates. \mathbf{S} in MRT operator and τ in SRT operator are related to the kinematic viscosity [19].

First, the steady flow field is solved by the single-phase solver. The fluid velocities within interstitial pores are regarded as converged (in steady state) when their averaged residual errors E_r , calculated as

$$E_r = (U_{n+1}^{\text{avg}} - U_n^{\text{avg}}) / U_n^{\text{avg}}, \quad (3)$$

are below 10^{-3} . U_n^{avg} denotes the average velocity at time step n . The steady velocity field is input to the reactive transport solver for advecting the solute concentrations. The steady flow field is updated if the pore structure alters by precipitation. To prevent the unnecessary calculations and increase simulation efficiency, two criterions were considered to decide updating time. First we track the porosity change at each time step. If the accumulative porosity change is over 0.1%, the flow field will be updated. Second, we set a fixed updating time interval (2000 time step) to get constant flow rate evolution. The relative permeability change can be calculated in a way that the updated pore geometry is exported at typical time steps and input to separate multiphase LBM solvers. A phase field approach is adopted to treat the two-phase flow [19]. In this multiphase solver, an order parameter ϕ is defined by using separate fluid density fields of wetting phase ρ_w and nonwetting phase ρ_n as

$$\phi = \frac{\rho_w - \rho_n}{\rho_w + \rho_n}. \quad (4)$$

The value of ϕ is constant in the bulk of each fluid phase and varies in the range $[-1, 1]$ at the diffusive fluid-fluid interface. The width of the interface is around two to three lattice units. The advection of the scalar density field (ρ_w and ρ_n) can be done by using the following LB equation for dimensionless density distribution g_i :

$$\begin{aligned}g_i^w(t + \Delta t, x + e_i \Delta t) &= g_i^{w(\text{eq})}(\rho_w(t, x), u(t, x)), \\ g_i^n(t + \Delta t, x + e_i \Delta t) &= g_i^{n(\text{eq})}(\rho_n(t, x), u(t, x)).\end{aligned}\quad (5)$$

The equilibrium distribution functions $g_i^{w, n(\text{eq})}$ are given in Toelke *et al.* [12]. The wetting tendency of the wall can be controlled by setting a virtual order parameter ϕ_{wall} on the solid lattice nodes to a value from -1 (nonwetting or hydrophobic) to 1 (wetting or hydrophilic) or somewhere in between. The target contact angle θ is able to be defined by the following

simple equation [20]

$$\cos \theta = \phi_{\text{wall}}. \quad (6)$$

The wettability implementation is numerically validated in our previous study [21]. No-slip boundary conditions are imposed at all solid nodes, including the precipitated minerals, using a half-way bounce-back scheme. A pressure gradient is imposed across the inlet and outlet. Implementation of these boundary conditions is discussed in Ref. [22].

C. Reactive transport solver

The carbonate precipitation process is represented by a two-component system of Ca^{2+} and CO_3^{2-} as



The precipitation rate is controlled by the changing Ca^{2+} and CO_3^{2-} concentrations in the fluid. For convenience, we here assume equilibrium conditions and consider only the Ca^{2+} concentration [9]. The reactive transport of the Ca^{2+} component is modeled by an advection-diffusion formula as

$$\frac{\partial C}{\partial t} = \nabla \cdot (D \nabla C) - \nabla \cdot (\mathbf{u}C) + R, \quad (8)$$

$$R = -k_T \frac{A}{M_H} \left(\frac{C - C_{\text{eq}}}{C_{\text{eq}}} \right), \quad (9)$$

where C is the Ca^{2+} concentration in the fluid. R is a source term denoting the rate at which CaCO_3 is produced by chemical reaction. \mathbf{u} in Eq. (8) is the steady velocity field derived by LBM, and D is the diffusion coefficient. C_{eq} in Eq. (9) represents the saturation concentration of Ca^{2+} , A/M_H is the specific reactive surface area parameter [9], and k_T is the rate constant of the chemical reaction at temperature T . The system is numerically solved by a FVM incorporating a total variation diminishing (TVD) scheme. The advection term of Eq. (8) is discretized as follows:

$$C_i^{n+1} = C_i^n - \frac{dt}{dx} (F_{i+1/2} - F_{i-1/2}), \quad (10)$$

$$F_{i+1/2} = u \left(C_i + \frac{1}{4}(1 + \phi) \tilde{\Delta}^+ C_i + \frac{1}{4}(1 - \phi) \tilde{\tilde{\Delta}}^+ C_{i-1} \right), \quad (11)$$

$$\tilde{\Delta}^+ C_{i-1} = \min \text{mod}(\Delta^+ C_{i-1}, \beta \Delta^+ C_i), \quad (12)$$

$$\tilde{\tilde{\Delta}}^+ C_i = \min \text{mod}(\Delta^+ C_i, \beta \Delta^+ C_{i-1}).$$

Here, the scalar flux $F_{i+1/2}$ across the cell is calculated by the Chakravarthy-Osher TVD [23] scheme, which effectively suppresses numerical diffusion. The subscript i represents the spatial grid index. dt is the time interval, determined by the Courant-Friedrichs-Lewy (CFL) stability conditions, and dx is the mesh size. The diffusion term of Eq. (8) is discretized by using a second-order central difference scheme. The FVM and LBM solvers are implemented on identical grid systems to avoid unnecessary interpolation. β in Eq. (12) is given as

$$\beta = \frac{(3 - \phi)}{(1 - \phi)}. \quad (13)$$

Here, parameter ϕ is set to be $1/3$ to apply the third-order upwind scheme. The Δ^+ with tilde denotes the flux limiter

defined by the min mod function which is given by

$$\min \text{mod}(a, b) = \begin{cases} a & |a| < |b| \\ b & |a| > |b| \\ 0 & ab \leq 0 \end{cases} \quad (14)$$

Constant flux and zero-gradient boundary conditions were imposed at the inlet and outlet, respectively.

D. Clogging model

The changes in pore structure resulting from carbonate precipitation were estimated by two clogging models. The first model uses chemical reaction theory described above to evaluate the local (node) volume variation of the precipitate. We introduce a mass variable M that records the amount of precipitated carbonate according to the chemical reaction in Eq. (9). The mass of deposited Ca^{2+} evolves as

$$\frac{\partial M_i}{\partial t} = \lambda c'_i, \quad (15)$$

where $\lambda = (k_T/c_{\text{eq}})(A/M_H)$ and $c'_i (=c - c_{\text{eq}})$ is the super-saturated concentration. The precipitated mass of CaCO_3 is explicitly updated after each time step as

$$M_i(t + dt) = M_i(t) + \lambda c'_i dt. \quad (16)$$

The time interval dt is used in the FVM solver for reactive transport. The volume of the precipitate V_p , obtained by dividing the calcite density by the mass M , is monitored at each node during each time step. When $V_p \geq dx \times dy \times dz$, the precipitate fills a single node, and the node is converted into solid phase. Once all precipitated solid nodes have been updated, the new solid nodes are stored in an additional matrix. To ensure exact mass conservation, the overrun of M at a precipitated node is evenly distributed among the neighboring fluid nodes.

The second model is introduced to generate a different precipitation pattern and to characterize the influence of different precipitation to permeability. We simply adjust the gray scale threshold to increase the proportion of solid nodes. This phenomenological method effectively narrows the pore space, and artificially reduces the porosity of the rock sample, and it removes the need to compute the Ca^{2+} concentration field.

III. VALIDATION SIMULATIONS

A. Single-phase permeability validation

The validation of single-phase permeability calculation followed the procedure introduced by Boek and Venturoli [24]. We impose a flow driven by a body force in the positive z direction of the rock. The body force g is related to the pressure drop ∇P by

$$\nabla P = \frac{P_i - P_o}{L} = g\rho, \quad (17)$$

where P_i and P_o are the pressures at the inlet and outlet, respectively, L is the length of the sample in the flow direction (distance between the inlet and outlet), and ρ is the fluid density. The absolute permeability k_{absolute} is calculated from

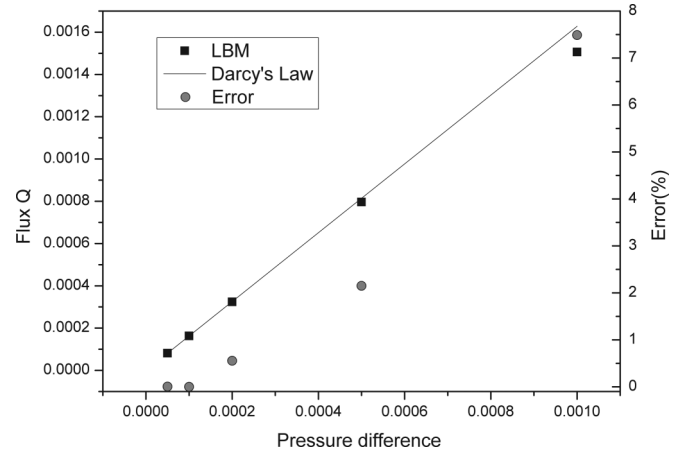


FIG. 2. Flux as a function of pressure difference across the domain. Deviation from Darcy's law becomes evident at higher pressure differences and fluxes. Both flux and pressure difference are expressed in lattice units.

the empirical Darcy's law as

$$k_{\text{absolute}} = -Q \frac{\mu}{A} \nabla P, \quad (18)$$

where Q is the volumetric flux, μ is the dynamic viscosity of the fluid, and A is the cross-sectional area of the sample. The permeability k_{absolute} is obtained by calculating the flux at different pressure drops (adjusting the body force values). The permeability has dimensions of area, and it is measured in units of Darcy (m^2). The simulation ran until it reached steady state, assessed by checking whether the average flux change per time step becomes lower than a given threshold 10^{-6} . We checked the dependence of the flux Q on the applied body force g . Here, we set relaxation parameter τ to 0.6, corresponding to a viscosity $\mu = 0.035$. This value of τ reportedly introduces the least deviation between analytical and simulation results of conductance in rectangular capillaries [24,25]. Darcy's law is known to be valid only in the laminar flow regime. For cases with high Reynolds number (Re), the inertial term becomes much more important, and the flux cannot be accurately predicted by Darcy's law. The flux Q is plotted as a function of body force g in Fig. 2. The flux linearly increases with increasing pressure gradient, but begins

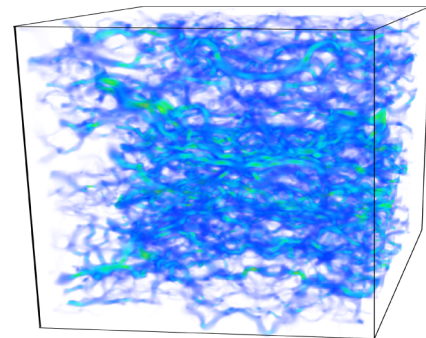


FIG. 3. (Color online) Fluid velocity distribution in Berea sandstone, obtained by a single-phase flow calculation. Yellow (light) and blue (dark) indicate regions of high and low velocity, respectively.

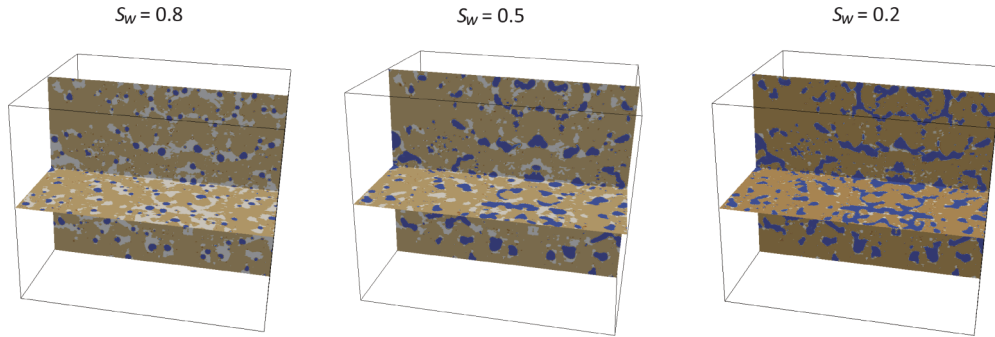


FIG. 4. (Color online) Nonwetting phase distributions in steady state simulations at wetting saturations (S_w) of 0.8, 0.5, and 0.2 (dark blue, nonwetting phase; white, wetting phase; light yellow, grains).

to deviate from Darcy’s law at higher flow rates due to the emergence of inertial effects which are incorporated in the LBM macroscopic flow models. The permeability can be predicted from the slope of a scatter plot of LBM results. The obtained absolute permeability of sample Berea sandstone is 769 mD. The velocity distribution of the pore space is illustrated in Fig. 3, from which the high velocity region and pore structures can be roughly confirmed.

B. Relative permeability validation

To assess the performance of our developed multiphase LBM solver, we validate the relative permeability curve calculated for the Berea sandstone rock model. The relative permeability is known to depend on pore structure, saturation, and on the balance between viscous and capillary forces. The relative permeability is calculated as

$$k_{nw} = -\frac{Q_{nw}\mu_{nw}}{k_{absolute}A \Delta P} \frac{L}{\Delta P}, \quad k_w = -\frac{Q_w\mu_w}{k_{absolute}A \Delta P} \frac{L}{\Delta P}, \quad (19)$$

where the subscripts “nw” and “w” refer to nonwetting fluid and wetting fluid, respectively. The Q_{nw} and Q_w are calculated at fixed saturation S_w .

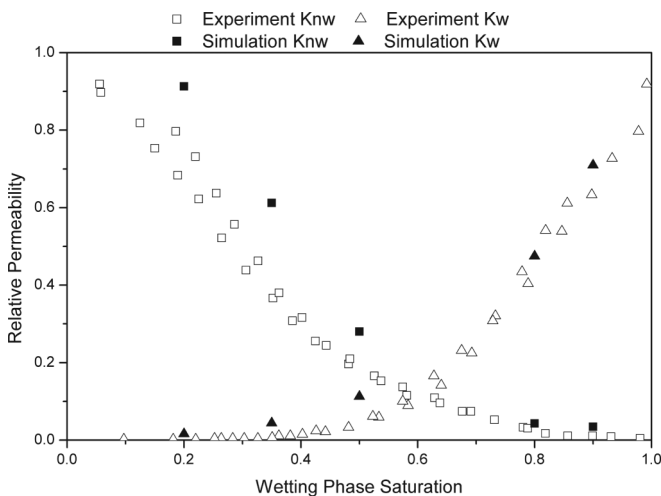


FIG. 5. Relative permeability of Berea sandstone; comparison between numerical simulation (black symbols) and laboratory experiment (open symbols) [26]. K_{nw} and K_w represent the relative permeability of nonwetting phase and wetting phase, respectively.

In this study, the relative permeabilities are computed by the steady state method. In this method, a mixture of two immiscible fluids is injected into the sample at specified constant flow rates. To transfer these conditions to our LB simulations, two phases of fluids are randomly distributed in the pore space according to the initially prescribed saturation. An imposed pressure gradient provides the body force that drives the fluids, as described above. Both surface tension σ and body force are adjusted to match the experimentally determined capillary number which is defined by

$$Ca = \frac{\mu \bar{U}}{\sigma}, \quad (20)$$

in which \bar{U} is the average velocity of the flow in pore space. Here, the capillary number is controlled at approximately 1×10^{-4} . The averaged flux of both fluids is calculated until the system reaches equilibrium.

The nonwetting phase distributions at wetting saturations of 0.2, 0.5, and 0.8 are shown in Fig. 4. Figure 5 compares the relative permeability under different saturation conditions with the experimental results [26]. In general, the experimental results are well matched by our simulation results except at low wetting saturations. Fluid movement within the rock is primarily influenced by the geometry of the pore space and

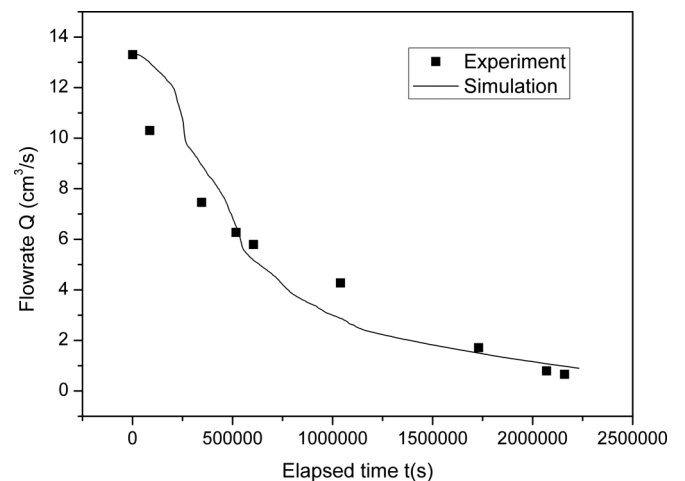


FIG. 6. Results of the flow rate evolution during carbonate precipitation in a bead pack model, obtained from numerical simulation (solid line, our data) and laboratory experiment (black squares, [9]).

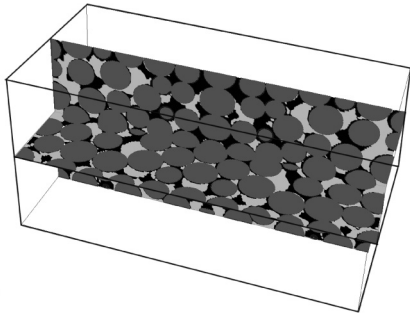


FIG. 7. Precipitated carbonate distribution in a bead pack model (light gray, solid beads; black, pore space; white, precipitated carbonate).

the capillary forces acting between the fluid phases and solid material. Because the microstructure of the Berea sandstone as well as the two fluid properties used in the experiment are not identical with our simulation, slight overestimation is observed at low wetting saturation conditions. We also realize that spurious velocities near the interface play an important role. Leclaire *et al.* [27] proved that the recoloring scheme used to keep the interface sharp largely affects the magnitude of the spurious velocities. These undesirable spurious velocities are always located near the interface. We realize that the large surface area of the nonwetting phase at low wetting saturation condition results in more spurious velocities and therefore causes errors as well.

C. Reactive transport model validation

Precipitation simulated by the reactive transport-based clogging model was validated on a bead pack model mimicking laboratory experiments [9]. In the experiment, fluid supersaturated with Ca^{2+} and CO_3^{2-} was injected into a rectangular column packed with glass beads. A digital version of the beads pack (initial porosity = 0.3) was created by the open-source discrete element method code YADE [28]. The domain size is $100 \times 100 \times 200$. The experiment was performed at constant average temperature (20.2 °C) and $p\text{H}$ (11.3) for 25 days. All parameters for the reactive transport solver, including the rate constant k_T , Ca^{2+} equilibrium concentration C_{eq} , and specific reactive surface area A , were set to the values specified in the

TABLE I. Physical properties of the CO_2 and water in the two-phase flow simulation. For stable computation, the density of CO_2 , and the viscosity of both fluids were assigned unrealistic values (the real values are listed in parentheses).

Property	Water	CO_2
Density (kg/m^3)	994	994 (668)
Viscosity (cP)	5.51 (0.551)	0.521 (0.0521)
IFT (mN/m)		35.0
Wettability (contact angle)		0°

experimental study [9]. The mesh size for this digital beads pack model is 0.1 mm, and the time interval in the reactive transport solver (0.0249 s) was sufficiently small to satisfy the CFL condition. The calculated flux was scaled to the Darcy flux measured in the experiment.

The simulated evolution of the flow rate during precipitation closely matched the experimental data (Fig. 6), confirming that the permeability decreases as Ca^{2+} and CO_3^{2-} precipitate into CaCO_3 . In addition, our simulation yielded the distribution of the precipitated carbonate inside the bead pack (Fig. 7). The heterogeneity of the precipitation process is related to the complicated flow field at the pore structure scale.

IV. RESULTS

Mineralization simulations were performed on the reconstructed digital pore model of the Berea sandstone. The domain size of this digital sample is $320 \times 320 \times 640$. The changing porosity and permeability resulting from carbonate precipitation is governed by the two clogging models described in the Section II. In terms of relative permeability calculations, we consider two-phase flow with water and liquid CO_2 at 2000 psi and 50 °C. Due to the model limitation, the density of CO_2 and water is assumed as same. Although the viscosity of both fluids is also different from the realistic values due to the stability problem, the ratio of viscosity agrees with real value (see Table I) [29,30].

A. Reactive transport clogging model

The precipitation process in the real pore structure was first simulated by the reactive transport model. The parameters and

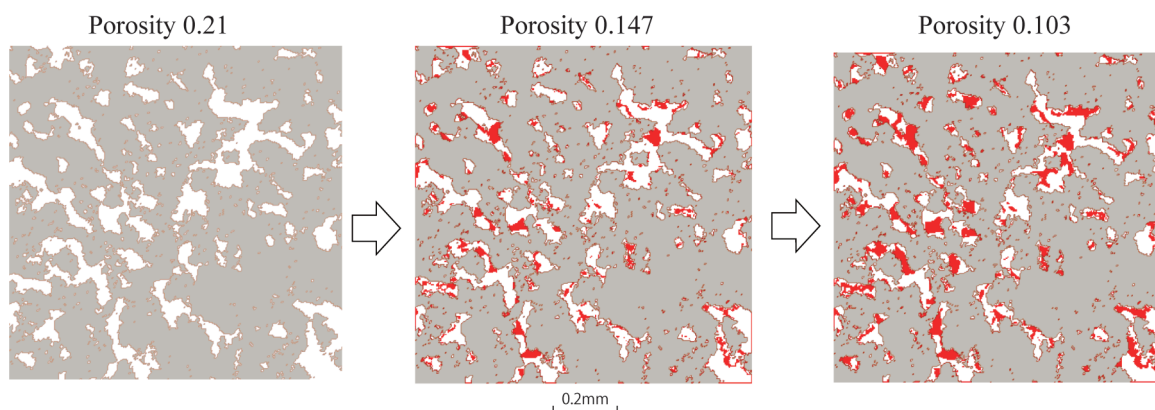


FIG. 8. (Color online) Evolution of pore structure resulting from precipitation at intersections perpendicular to the flow direction (light gray, original grain; dark red, precipitated regions).

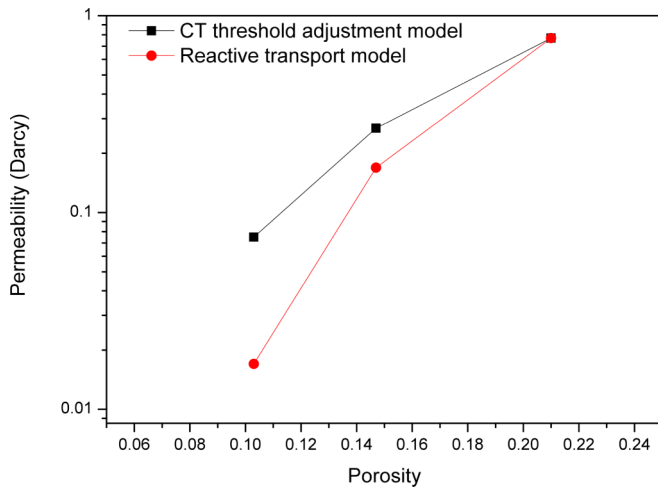


FIG. 9. (Color online) Evolution of absolute permeability as the porosity is altered by precipitation (0.21–0.103). Permeability was calculated by the two clogging models: CT threshold adjustment (black) and reactive transport (light red).

boundary conditions which were used to validate the model in Sec. III C were adopted again. With these ideal conditions, precipitation reduces the porosity by 50% in approximately 20 days. Notably, the precipitation is unevenly distributed (Fig. 8), and it preferentially occurs in relatively narrow pore bodies. The permeability calculations were rerun on evolved pore structures with selected porosities (14.7 and 10.3). The absolute permeability decreased from its original value (769 mD) to 169 and 11 mD at porosities of 14.7 and 10.3, respectively (Fig. 9). In the two-phase flow simulation, the relative permeability of the nonwetting phase significantly decreased after deposition [Fig. 10(a)]. Under the lowest wetting saturation condition, the relative permeability was reduced by 47.9% and 68.5% at porosities of 14.7 and 10.3, respectively. Conversely, in high wetting saturation condition, the relative permeability of the wetting phase decreased by approximately 20% at both porosities. Comparing the velocity

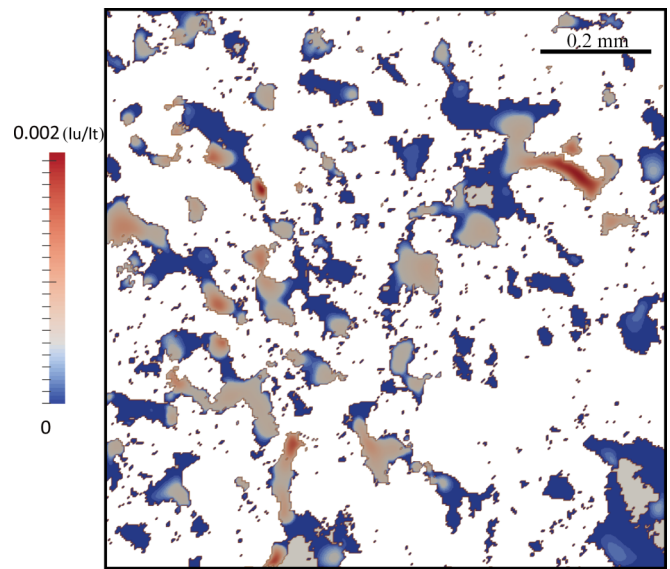
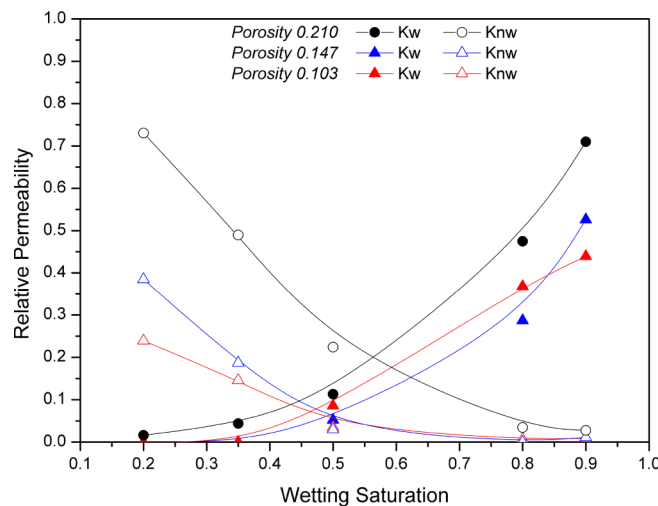


FIG. 11. (Color online) Velocity field at intersections perpendicular to the flow direction. The color scale represents the velocity magnitude in lattice units (lu, lattice unit; lt, lattice time), where red and blue denote high and low velocity, respectively.

magnitude distribution map (Fig. 11) with the precipitation distribution (Fig. 8) at the same intersections, we observe that precipitation mainly occurs on pore bodies subjected to high fluid velocities. However, precipitation position does not exactly coincide with sites of high velocity, but instead principally locates around sites of large velocity. Therefore, it appears that the sites of mineral deposition depend on both the velocity field and the pore structure.

B. CT image threshold adjustment model

The pore space size was artificially reduced by adjusting the gray scale threshold, thereby mimicking the mineral precipitation around grains. The rock area occupied by solid

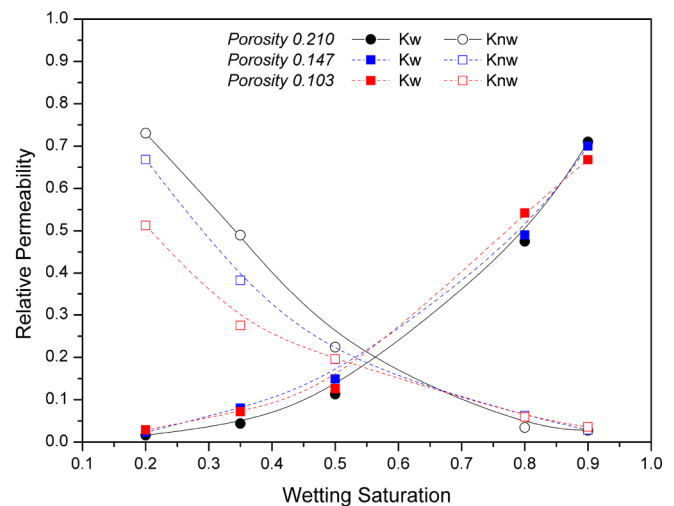


FIG. 10. (Color online) Evolution of relative permeability as the porosity of Berea sandstone is altered by the two different clogging models (0.210–0.103). Knw and Kw represent the relative permeability of nonwetting phase and wetting phase, respectively.

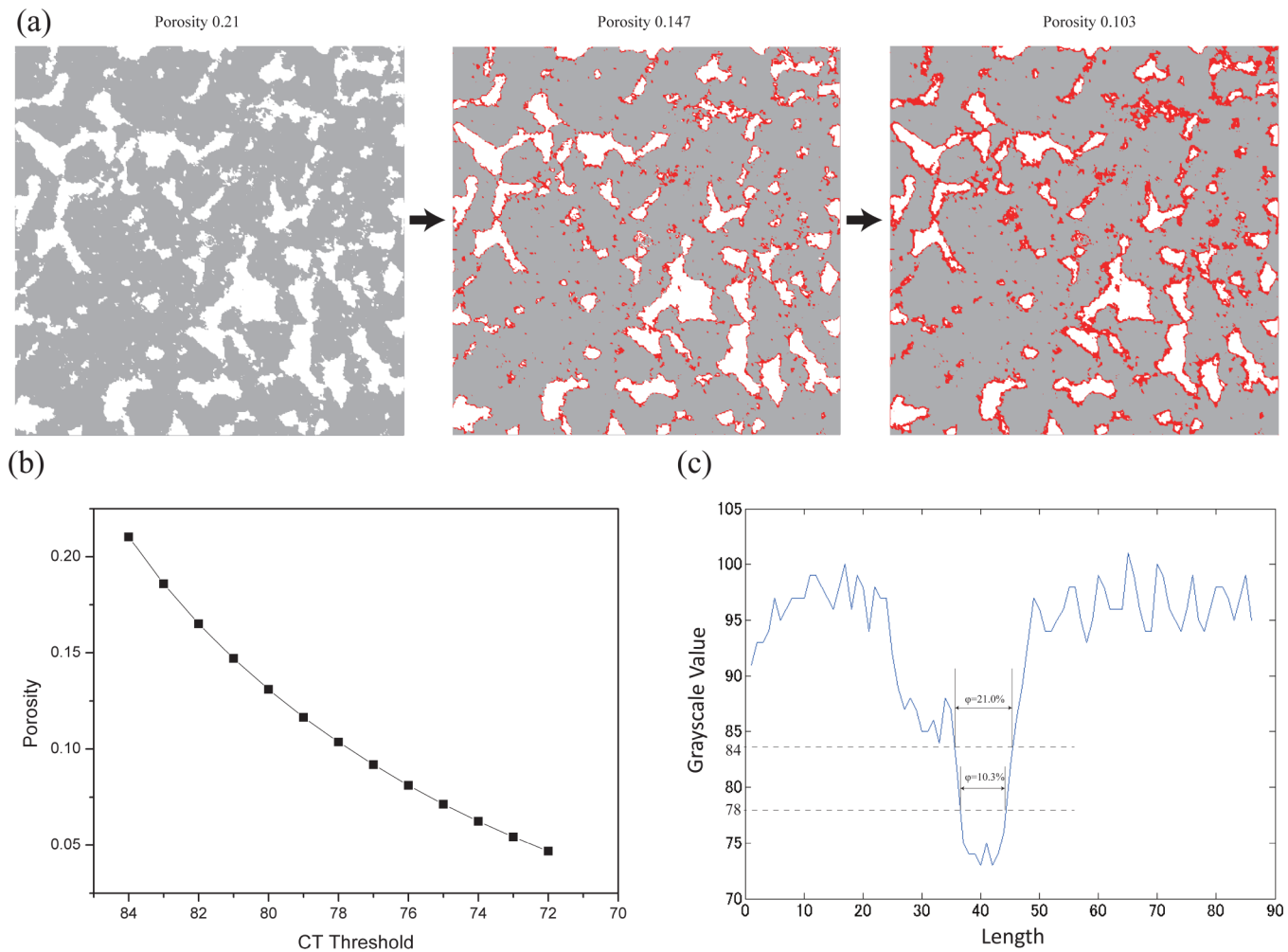


FIG. 12. (Color online) Illustration of CT threshold adjustment clogging model: (a) Evolution of pore space distribution as CT threshold is lowered (from left to right); original solid areas are depicted in light gray and precipitated minerals are represented in dark red. (b) Dependence of porosity on CT threshold. (c) CT gray scale value along the x direction across a selected single pore body. Thresholds 84 and 78 correspond to the porosities of 21.0% and 10.3%, respectively.

phase was observed to increase with decreasing threshold value (Fig. 12). Initially, small isolated pores were filled. The large-scale pore boundary grew without directional preference. The relationship between porosity (void fraction) and CT threshold is plotted in Fig. 12(b). Intuitively, increase of the CT threshold will reduce the space occupied by pores and consequently decrease the rock porosity. The CT values along the x direction of a selected single pore [Fig. 12(c)] indicate that gray scale changes gradually from the original boundary to the center of the pore. The width of the pore is $32.1 \mu\text{m}$ for threshold 84 and $24.6 \mu\text{m}$ for threshold 78, corresponding to the porosity 21.0% and 10.3%, respectively. Therefore with decreasing the CT threshold value, we can mimic the process that pore shrinks (minerals grow from the grain surface) and finally disappears. The permeabilities of three pore geometries—original porosity 21.0% and reduced porosities 14.7% and 10.3%—were computed by the single and two-component LB solvers, respectively. As expected, the absolute permeability decreased from 769 mD to 268 and 103 mD at porosities of 14.7 and 10.3, respectively (Fig. 9). The relative permeability calculation [Fig. 10(b)] yielded no

noticeable changes in the wetting phase, while the relative permeability of the nonwetting phase decreased with reduced porosity only at wetting saturations below 0.5.

V. DISCUSSION

A. Evolution of relative permeability resulting from precipitation

The results of both clogging models indicate that the relative permeability of the nonwetting phase is significantly influenced by changes in the pore structure resulting from precipitation. The effect is particularly severe under low wetting saturation conditions. In this condition, since the nonwetting phase occupies most of the pore spaces, its movement is suppressed by the increased capillary pressure determined by the pore sizes. The relative permeability is much less sensitive to pore structure under highly saturated wetting conditions. Because the nonwetting fluid inside the pore structure separates into droplets, the fluid can enter the pore when the droplet size is smaller than the pore throat.

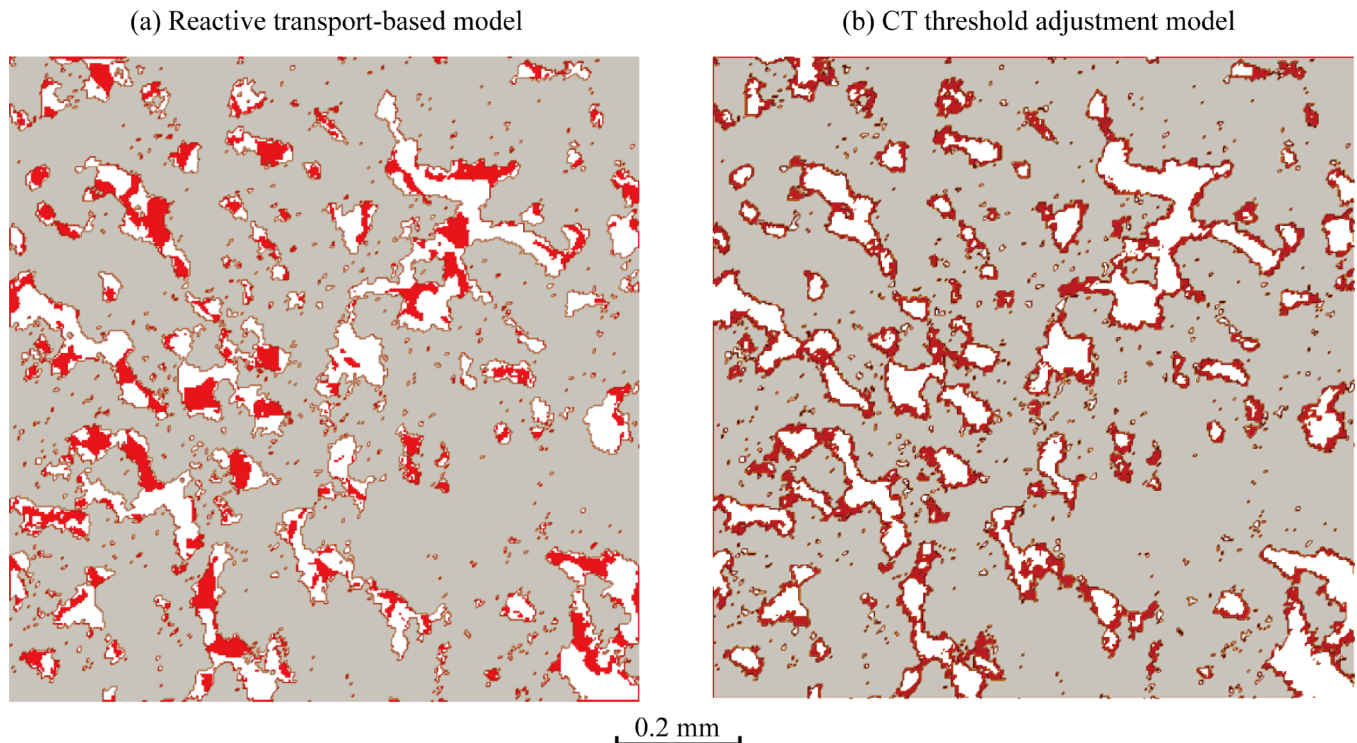


FIG. 13. (Color online) Comparison of the precipitation patterns yielded by the two clogging models (light gray, original grain; dark red, precipitated regions).

Conversely, the relative permeability of the wetting phase is relatively invariant under all wetting saturation conditions. Since the grain is set to be totally wettable, a wetting layer presumably covers the solid pore boundaries [19], and the wetting phase does not accumulate at narrowed pore throats, as occurs in the nonwetting phase. Relative permeability is also regarded as highly sensitive to the wettability of the grain and surface tension, which are retained constant in the present study. Therefore, we conclude that decreasing the pore space via mineral deposition significantly impacts on the relative permeability of the nonwetting phase, while exerting slight influence on the wetting phase.

B. Comparison of the two clogging models

The proposed clogging models display different characteristics in their deposition patterns (Fig. 13). In the CT threshold adjustment model, pore space shrinks along the boundary walls, and the artificially deposited parts are approximately uniform [Fig. 13(b)]. In contrast, precipitate growth in the reactive transport clogging model favors certain locations and directions [Fig. 13(a)]. The reactive clogging mechanism is based on the concentration of the reactive components, while the advection and diffusion of the concentration field is controlled by the flow field, pore structure, and connectivity. Therefore, the deposition behavior depends on both the flow velocity distribution and variation in pore geometry.

Both the absolute and relative permeabilities are affected by the mineral deposition patterns. The reactive transport clogging model outputs a much smaller permeability because the deposition is unevenly distributed in this model (Fig. 9). Some precipitate partially blocks the pore spaces,

dividing the pore bodies into individual smaller pores, and destroying the homogeneous property of the Berea sandstone. This transition from homogeneity to heterogeneity decreases the relative permeability of both wetting and nonwetting phases (Fig. 10). In comparison, the CT threshold adjustment clogging model maintains the homogeneous property, and only the relative permeability of the nonwetting phase is reduced by the shrinking pore space. The proposed reactive transport model can potentially be extended to simulate multicomponent systems and incorporate more complex reaction terms that characterize real reaction situations.

VI. SUMMARY

The changes in pore geometry and relative permeability induced by carbonate precipitation in porous media were investigated by a transport simulation model constructed at the pore scale. The method calculates the relative permeability by a multiphase flow solver, and it includes two precipitation models for simulating pore clogging. The accuracy of our proposed model was validated on Darcy's law and relative permeability calculations, and by reactive transport simulation through a digitized bead pack. The method proved sufficiently accurate for calculating both single- and two-phase flow coupled with solute transport in porous media. Simulations were performed on a digital rock model reconstructed from micro-CT scanned images of a real Berea sandstone sample. For the reactive transport precipitation model, we used the exact ideal conditions as for the experiment by Yoo *et al.* [9] to intentionally generate the mineralization process with supersaturated solution. Therefore, precipitation will occur

during injection in a very short time scale (several weeks). Comparing the precipitated and initial pore geometries, the two clogging methods were found to yield different depositional and growth precipitation patterns. The clogging model based on reactive transport calculates an uneven precipitate distribution that destroys the rock homogeneity, with consequent marked decreases in both absolute and relative permeability. Conversely, the CT threshold adjustment model gives approximately uniform precipitate distribution. However, in both clogging models, pore structural changes induced by carbonate precipitation significantly influenced the absolute permeability, and that pore space reduction affects the relative permeability of the nonwetting phase considerably more than that of the wetting phase. The evolution of relative permeability obtained by our numerical method is an important parameter, which can be a direct input to conventional large-

scale reservoir simulators to investigate the outcome of the injected CO₂ and to evaluate the injectivity mediated by the mineralization process.

ACKNOWLEDGMENTS

The authors are grateful for the useful advice and suggestions from Dr. Jianhui Yang. The authors would like to thank the anonymous reviewers for their valuable comments and constructive discussion to improve the quality of this paper. This study was partially supported by a Grant-in-Aid for Research Activity Start-up from the JSPS (Grant No. 26887028). The authors gratefully acknowledge the support of the International Institute of Carbon-Neutral Energy Research (WPI-I2CNER), sponsored by the Japanese Ministry of Education, Culture, Sports, Science and Technology.

-
- [1] O. D. Bert Metz, Heleen de Coninck, Manuela Loos, and Leo Meyer, *IPCC Special Report on Carbon Dioxide Capture and Storage* (Cambridge University Press, Cambridge, 2005).
- [2] J. Hostomsky and A. G. Jones, *J. Phys. D: Appl. Phys.* **24**, 165 (1991).
- [3] R. Shiraki and S. L. Brantley, *Geochim. Cosmochim. Acta* **59**, 1457 (1995).
- [4] D. Pontoni, J. Bolze, N. Dingenouts, T. Narayanan, and M. Ballauff, *J. Phys. Chem. B* **107**, 5123 (2003).
- [5] J. Rieger, T. Frechen, G. Cox, W. Heckmann, C. Schmidt, and J. Thieme, *Faraday Discuss.* **136**, 265 (2007).
- [6] M. Kellermeier, E. Melero-García, F. Glaab, R. Klein, M. Drechsler, R. Rachel, J. M. García-Ruiz, and W. Kunz, *J. Am. Chem. Soc.* **132**, 17859 (2010).
- [7] P. O. Mangane, P. Gouze, and L. Luquot, *Geophys. Res. Lett.* **40**, 4614 (2013).
- [8] L. Chen, Q. Kang, B. A. Robinson, Y.-L. He, and W.-Q. Tao, *Phys. Rev. E* **87**, 043306 (2013).
- [9] S.-Y. Yoo, Y. Kuroda, Y. Mito, T. Matsuoka, M. Nakagawa, A. Ozawa, K. Sugiyama, and A. Ueda, *Appl. Geochem.* **30**, 67 (2013).
- [10] J. Tölke, C. Baldwin, Y. Mu, N. Derzhi, Q. Fang, A. Grader, and J. Dvorkin, *The Leading Edge* **29**, 68 (2010).
- [11] C. Pan, M. Hilpert, and C. T. Miller, *Water Resour. Res.* **40**, W01501 (2004).
- [12] J. Tölke, S. Freudiger, and M. Krafczyk, *Comput. Fluids* **35**, 820 (2006).
- [13] P. Meakin and A. M. Tartakovsky, *Rev. Geophys.* **47**, RG3002 (2009).
- [14] C. I. Steefel, D. J. DePaolo, and P. C. Lichtner, *Earth Planet. Sci. Lett.* **240**, 539 (2005).
- [15] Q. Kang, P. C. Lichtner, and D. Zhang, *J. Geophys. Res.: Solid Earth* **111**, B05203 (2006).
- [16] Q. Kang, I. N. Tsimpanogiannis, D. Zhang, and P. C. Lichtner, *Fuel Process. Technol.* **86**, 1647 (2005).
- [17] P. L. Bhatnagar, E. P. Gross, and M. Krook, *Phys. Rev.* **94**, 511 (1954).
- [18] S. Chen and G. D. Doolen, *Annu. Rev. Fluid Mech.* **30**, 329 (1998).
- [19] B. Ahrenholz, J. Tölke, P. Lehmann, A. Peters, A. Kaestner, M. Krafczyk, and W. Durner, *Adv. Water Res.* **31**, 1151 (2008).
- [20] M. Latva-Kokko and D. H. Rothman, *Phys. Rev. E* **72**, 046701 (2005).
- [21] F. Jiang, T. Tsuji, and C. Hu, *Transp. Porous Med.* **104**, 205 (2014).
- [22] T. Ramstad, N. Idowu, C. Nardi, and P.-E. Øren, *Transp. Porous Med.* **94**, 487 (2012).
- [23] S. Chakravarthy and S. Osher, in *23rd Aerospace Sciences Meeting* (American Institute of Aeronautics and Astronautics, Reston, 1985).
- [24] E. S. Boek and M. Venturoli, *Comput. Math. Appl.* **59**, 2305 (2010).
- [25] M. Venturoli and E. S. Boek, *Physica A* **362**, 23 (2006).
- [26] M. J. Oak, L.E. Baker, and D. C. Thomas, *J. Pet. Technol.* **42**, 8 (1990).
- [27] S. Leclaire, M. Reggio, and J.-Y. Trépanier, *Appl. Math. Modell.* **36**, 2237 (2012).
- [28] J. Kozicki and F. Donzé, *Comput. Meth. Appl. Mech. Eng.* **197**, 4429 (2008).
- [29] L.-B. Ouyang, *The Open Petrol. Eng. J.* **4**, 13 (2011).
- [30] P. Chiquet, J.-L. Daridon, D. Broseta, and S. Thibeau, *Energy Convers. Manage.* **48**, 736 (2007).